Constraining cosmic ray acceleration in young star clusters using multi-wavelength observations

Siddhartha Gupta,[1,2]⋆ Biman B. Nath[1] and Prateek Sharma[2]

[1]*Raman Research Institute, Sadashiva Nagar, Bangalore 560080, India*
[2]*Joint Astronomy Programme and Department of Physics, Indian Institute of Science, Bangalore 560012, India*

ABSTRACT

We use 1D and 3D two-fluid cosmic ray (CR) hydrodynamic simulations to investigate the role of CRs in the vicinity of a compact young star cluster. We model a self-gravitating cloud (density profile $\rho \propto r^{-1}$), include important thermal and non-thermal processes, and explore two different CR injection scenarios. We show that if internal shocks in the wind-driving region are the main site for CR acceleration, then the resulting γ-ray luminosity (L_γ) can reach ≈ 5 per cent of the mechanical luminosity (L_w), independent of the fraction of wind energy (~ 1–20 per cent) injected into CRs. In contrast, if the forward/reverse shock of a bubble is the injection site then L_γ increases linearly with the CR injection fraction, as expected analytically. We find that the X-ray luminosity (L_x) in the forward/reverse shock injection scenario is $\gtrsim 10^{-3} L_w$, which is ~ 10 times larger than in the central wind-driving injection case. We predict the corresponding range of the synchrotron radio luminosity. We show how multi-wavelength observations can constrain the CR parameters. Comparing the predicted multi-wavelength luminosities with those of 30 Doradus and Westerlund 2 we identify the reverse shock as the most probable CR injection site. We do not find significant dynamical impact of CRs in our models.

Key words: hydrodynamics – ISM: bubbles – cosmic rays – galaxies: star clusters: general.

1 INTRODUCTION

Star clusters are among the most fundamental objects in a galaxy. They are located in the core of dense molecular clouds and contain several thousand solar mass. The stars energize the surrounding medium, leading to gas expulsion and the formation of interstellar bubbles (ISBs). These star clusters are the laboratory to study phenomena such as star formation and stellar feedback which are important components to understand galaxy evolution (for reviews see de Grijs 2010; Portegies Zwart, McMillan & Gieles 2010; Longmore et al. 2014).

The theoretical modelling of ISBs serves as a standard scenario for the wind and ISM interaction (Weaver et al. 1977). Observations in X-rays, ultraviolet and infrared (e.g. Chu et al. 2003; Townsley et al. 2006; Lopez et al. 2014) have helped in our understanding of ISBs. Recent works have attempted to relax some of the assumptions in the standard scenario, for example, include the effect of different forms of pressure other than thermal pressure, or include the effect of spatial distribution of stars. It has been found that the dynamics of ISBs strongly depend on the clustering of stars and on the ambient density (e.g. Krause et al. 2013; Nath & Shchekinov 2013; Sharma

et al. 2014; Kim & Ostriker 2015; Martizzi, Faucher-Giguére & Quataert 2015; Vasiliev, Shchekinov & Nath 2017; Yadav et al. 2017). The effect of stellar radiation has also been studied (Harper-Clark & Murray 2009; Silich & Tenorio-Tagle 2013; Dale, Ercolano & Bonnell 2013). It has been shown that radiation pressure can boost gas expulsion in the early phase ($\lesssim 1$ Myr) whereas the late time evolution is governed by the mechanical energy injection and photo-heating (Gupta et al. 2016). There is another promising driving mechanism, namely, the pressure due to relativistic particles such as cosmic rays (CRs), whose effects are yet to be understood in detail.

Star-forming regions have been thought to be efficient sites for CR acceleration (Knödlseder 2013; Bykov 2014; Aharonian, Yang & de Oña Wilhelmi 2018). Several ISBs have been identified as powerful sources of gamma-rays (hereafter γ-rays). Ackermann et al. (2011) found that the Cygnus OB association is quite bright in GeV range (see also Tibaldo et al. 2013). Yang, de Oña Wilhelmi & Aharonian (2018) reported γ-ray emission in Westerlund 2. High-energy photons have also been detected from the large magellanic cloud (LMC). It has been reported that a massive star cluster, 30 Doradus, produces both GeV and TeV photons (Abdo et al. 2010; Abramowski et al. 2015). In a few cases, the γ-ray luminosity is ~ 1 per cent of the wind mechanical power, and it is almost comparable to the X-ray luminosity (cf. Table 1). Furthermore, Hughes

⋆ E-mail: siddhartha@rri.res.in

et al. (2007) concluded that 30 Doradus dominates the radio continuum emission in LMC at 1.4 GHz (see also Murphy et al. 2012; Foreman et al. 2015). These emissions occur when relativistic particles interact with the magnetic field and matter, and confirm the presence of CRs in ISBs. It is then reasonable to ask to what extent CRs affect the dynamics and evolution of ISBs.

There is yet another motivation to study the effect of CRs on ISBs. At a larger length-scale, it has been suggested that CRs can dynamically affect galactic winds (Booth et al. 2013; Salem & Bryan 2014; Simpson et al. 2016; Wiener, Pfrommer & Oh 2017). However, the detailed physics is not clearly understood. First, changing the adiabatic index of the gas from 5/3 to 4/3 (i.e. replacing thermal pressure by CR pressure) *reduces* the size of ISBs (e.g. see equation 4 in Gupta et al. 2018; also see Chevalier 1983). Secondly, diffusion of CRs would tend to *decrease* the pressure gradient, and therefore *reduce* the dynamical effect of CRs. We propose to study these processes in an ISB, which may help us to understand the effects at a larger length-scale.

In an earlier work, we studied the effect of CRs in an idealized ISB (Gupta et al. 2018). We found that the effect of CRs mainly depends on the CR injection region, diffusion coefficient and the shock Mach number. CRs can be injected in two different ways. In one case, CRs are injected at spatially resolved shocks whereas in the other case, it is assumed that a small fraction (∼10 per cent) of the wind/supernovae energy directly goes to CRs via internal shocks (these internal shocks may originate due to stellar flares, colliding winds and supernovae which are difficult to resolve in numerical simulations). The basic difference in (spatially resolved) shock injection and central injection of CRs is that, in the latter case, the back reaction from CRs at the shock can modify the thermodynamic properties of the shock when the Mach number exceeds $\gtrsim 12$ (Drury & Völk 1981; Drury & Falle 1986; Becker & Kazanas 2001). In this case most of the upstream kinetic energy goes into CRs. This is how diffusive shock acceleration is captured in a two-fluid model. We estimated various relevant time-scales for the CR affected bubbles (see sections 2.2 and 4.2 in Gupta et al. 2018). We showed that CR-dominated ISBs may contain comparatively cool thermal plasma (temperature ∼$10^{6.5}$ K), even in the absence of thermal conduction (TC; which can also reduce the interior temperature of an ISB).

In this paper, we extend our work to determine the multi-wavelength signatures of ISBs arising from the presence of CRs, with the help of 1D and 3D numerical simulations. This will help us to compare our findings with observations of ISBs in different wavelengths, and to constrain the CR injection parameters.

We focus on the early evolution ($\lesssim 4$ Myr) when mechanical wind from a compact star cluster can form a reverse (termination) shock. We do not include supernova explosion (e.g. Sharma et al. 2014; Kim & Ostriker 2015; Vasiliev et al. 2017; Yadav et al. 2017) or large spatial separation of stars, which may change the evolution and structure of the ISBs. We start with an analytic estimate of different luminosities for a two-fluid ISB in Section 2. In Section 3 we discuss some recent results from ISB observations. This helps us to set-up our simulation, as discussed in Section 4. The results are presented in Sections 5 and 6, and summarized in Section 7.

2 ANALYTICAL ESTIMATES

We consider an idealized two-fluid model of an ISB (for details, see Gupta et al. 2018). We wish to estimate the γ-ray, X-ray and radio luminosities, considering that CRs are being accelerated in an ISB.

2.1 γ-ray

The nature of γ-ray emission depends on the interaction mechanism between CRs and matter (Mannheim & Schlickeiser 1994).

2.1.1 Hadronic origin

To estimate γ-ray luminosity due to hadronic interaction, we use the analytical prescription of Pfrommer & Enßlin (2004), which is briefly discussed below.

The γ-ray luminosity in ($E_{\gamma 1} - E_{\gamma 2}$) energy band can be estimated using

$$
\begin{aligned}
L_\gamma^H &= \int_V dV \int_{E_{\gamma 1}}^{E_{\gamma 2}} dE_\gamma \, E_\gamma \, q_\gamma(n_N, e_{cr}, E_\gamma) \\
&= \int_V dV \, n_N \, e_{cr} \left[\int_{E_{\gamma 1}}^{E_{\gamma 2}} dE_\gamma \, E_\gamma \, \tilde{q}_\gamma(E_\gamma) \right],
\end{aligned} \tag{1}
$$

where $q_\gamma = dN/(dt \, dV \, dE_\gamma)$ is the number of γ-ray photons emitted per unit volume per unit time per unit energy, which is proportional to n_N (the number density of target nucleon) and e_{cr} (the CR energy density), and $\int_V dV$ is the volume of the emitting region. The function $\tilde{q}_\gamma$ is given as

$$
\tilde{q}_\gamma = \left[\frac{\sigma_{pp} c \left(\frac{E_{\pi 0}}{GeV} \right)^{-\alpha_\gamma} \left[\left(\frac{2E_\gamma}{E_{\pi 0}} \right)^{\delta_\gamma} + \left(\frac{2E_\gamma}{E_{\pi 0}} \right)^{-\delta_\gamma} \right]^{-\alpha_\gamma/\delta_\gamma}}{\xi^{\alpha_\gamma - 2} \left(\frac{3\alpha_\gamma}{4} \right) \frac{E_p}{2(\alpha_p - 1)} \left(\frac{E_p}{GeV} \right)^{1-\alpha_p} \beta\left(\frac{\alpha_p - 2}{2}, \frac{3-\alpha_p}{2} \right)} \right]. \tag{2}
$$

Here $E_p/E_{\pi 0}$ is the rest mass energy of proton/pions (π^0), α_p and α_γ are the spectral indices of the incident CR protons and emitted γ-ray photons, respectively, $\delta_\gamma = 0.14\alpha_\gamma^{-1.6} + 0.44$ is the spectral shape parameter and $\sigma_{pp} = 32(0.96 + e^{4.4 - 2.4\alpha_\gamma})$ mbarn (see equations 8, 19–21 in Pfrommer & Enßlin 2004).

From equation (1), we find that the result of the integration from 0.1 to 200 GeV energy is ≈1.1×10^{-16} cm³ s⁻¹ and it depends weakly (error <20 per cent) on the choice of α_p or α_γ (2.1−2.5) when $\alpha_\gamma = \alpha_p$ (Dermer 1986). The γ-ray spectrum beyond 200 GeV differs from model to model, and we have, therefore, excluded it from our analysis. We thus obtain the γ-ray luminosity in ≈(0.1 − 100) GeV band:

$$
L_\gamma^H \simeq 1.1 \times 10^{-16} \int_V \left(\frac{dV}{cm^3} \right) \left(\frac{n_N}{cm^{-3}} \right) \left(\frac{e_{cr}}{erg \, cm^{-3}} \right) \, erg \, s^{-1}. \tag{3}
$$

Clearly L_γ is directly proportional to the target nucleon (n_N) and the CR energy density (e_{cr}), and therefore, the γ-ray emission arises from the denser region of the ISBs, e.g. the swept-up ambient medium (shell).

Consider the ambient density profile to be $\rho(r) = \rho_c (r_c/r)^s$ where ρ_c/r_c is the core density/radius of the ambient medium. We denote the CR pressure fraction in the shell as $W_{sh} = P_{cr}/(P_{th} + P_{cr})$ [$P_{cr/th}$ is the volume-averaged CR/thermal pressure in the shell]. From the self-similar evolution of the bubble we obtain

$$
L_\gamma^H = A \, W_{sh} \, L_w^{(5-2s)/(5-s)} \left(\rho_c r_c^s \right)^{5/(5-s)} t_{dyn}^{(5-4s)/(5-s)} \tag{4}
$$

where

$$
A = \frac{13.2\pi \times 10^{-16}}{m_H} \left(\frac{21 - 6s}{(5-s)^2(3-s)^2} \right)
$$

$$
\times \left[\frac{(\gamma - 1)(5-s)^3(3-s)}{4\pi\{(63 - 18s)\gamma + s(2s+1) - 28\}} \right]^{(5-2s)/(5-s)}. \tag{5}
$$

Here we have used equations (4) and (5) in Gupta et al. ([2018](#)) to estimate the shell volume $\approx \Delta V$ ($=4\pi R^2 \Delta R$, ΔR is the shell width and R is the radius of the ISB)[1] and target density n_N ($\approx 4 \times \rho(R)/m_H$). We also have taken CR energy density $e_{cr} = P_{cr}/(\gamma_{cr} - 1)$ where $\gamma_{cr} = 4/3$.

Equation (4) shows that, for a fixed[2] W_{sh}, the time evolution of γ-ray luminosity depends on the ambient density power-law index 's'. If $5 > s > 5/4$, then L_γ^H decreases with time. This is reasonable because the density falls so rapidly that only small column density targets are available for hadronic interaction. For $s < 5/4$, L_γ^H is an increasing function of time. This means that, in principle, one can explain the observed luminosity with a small W_{sh} by taking longer dynamical time. However, in practice, the dynamical time is not a free parameter, because it is well constrained by the bubble radius and shell speed. Therefore, the modelling of the ambient density profile is crucial to interpret γ-ray observation.

2.1.2 Leptonic origin

Low-energy photons ($\ll$ GeV), which come from stars and/or cosmic microwave background (CMB) radiation, can gain significant energy via inverse Compton scattering with relativistic electrons. These secondary photons can be a possible source of γ-rays in ISBs.

Suppose the incident photons are dominated by stellar radiation with energy $E_{incident} \sim 0.01-100$ eV (far infrared to extreme UV). The corresponding Lorentz factor of relativistic electrons, required to enhance the energy of stellar photons to E_{obs} ($\approx 0.1-100$ GeV), is spread over $\Gamma \approx (E_{obs}/E_{incident})^{1/2} \sim 10^3(\Gamma_{min}) - 10^6(\Gamma_{max})$. Assuming the number density distribution of relativistic electrons is $n(\Gamma) = \kappa_1 \Gamma^{-p}$ ($p \approx 2.2$ is the spectral index of relativistic electrons), we estimate the γ-ray luminosity (L_γ^{IC}) from (see equation 7.21 in Rybicki & Lightman [1979](#))

$$L_\gamma^{IC} = \int_V dV \left[\frac{4}{3} \sigma_T c \, e_{ph} \kappa_1 \frac{\Gamma_{max}^{3-p} - \Gamma_{min}^{3-p}}{3-p} \right], \qquad (6)$$

where e_{ph} is the stellar radiation energy density and σ_T is the Thomson cross-section. The normalization constant κ_1 is obtained from the energy density of CR electron e_{cr_e} as

$$\kappa_1 \approx \frac{e_{cr\_e}}{m_e c^2}(p-2) \left[\frac{1}{\Gamma_L^{p-2}} - \frac{1}{\Gamma_U^{p-2}} \right]^{-1}. \qquad (7)$$

Here, the lower and upper cutoff of Lorentz factor can be set to $\Gamma_L \to 1$ and $\Gamma_U \to \infty$. We assume the energy density of relativistic electrons $e_{cr\_e} = e_{cr}(m_e/m_p)^{(3-p)/2}$ (Persic & Rephaeli [2014](#)). For $p \approx 2.2$, this gives $e_{cr\_e} \approx 0.05 \, e_{cr}$.

The stellar radiation energy density (e_{ph}) depends on the distance from stars and radiation luminosity (L_{rad}). Assuming that the stars are confined in a small region and that the total radiation luminosity $L_{rad} \sim 500 L_w$ (L_w is the wind power; Leitherer et al. [1999](#)), e_{ph} at a distance r can be obtained from

$$e_{ph}(r) = \frac{L_{rad}}{4\pi r^2 c}$$
$$\approx 435 \left(\frac{L_w}{5 \times 10^{38} \mathrm{erg\, s^{-1}}} \right) \left(\frac{r}{10 \mathrm{pc}} \right)^{-2} \mathrm{eV\, cm^{-3}}, \qquad (8)$$

which is much larger than the energy density in CMB photons ~ 0.3 eV cm^{-3}. Using equation (6), we find that the γ-ray luminosity in $0.1-100$ GeV energy due to inverse Compton scattering is

$$L_\gamma^{IC} \approx 172 \times 10^{-16} \left(\frac{L_w}{5 \times 10^{38} \mathrm{erg\, s^{-1}}} \right)$$
$$\times \left[\int_V dV \left(\frac{r}{10 \mathrm{pc}} \right)^{-2} e_{cr} \right] \mathrm{erg\, s^{-1}}, \qquad (9)$$

where dV and e_{cr} are in CGS units.

Taking[3] $n_N \approx 4\rho_c(r_c/r)^s/m_H$ where $\rho_c = 220 \, m_H$ cm^{-3}, $r_c = 5$ pc and $s = 1$ (cf. Fig. [1](#)), equations (3) and (9) give the ratio of hadronic to Leptonic γ-ray luminosity:

$$\frac{L_\gamma^H}{L_\gamma^{IC}} \approx 2.6 \left(\frac{\rho_c}{220 m_H \mathrm{cm^{-3}}} \right) \left(\frac{L_w}{5 \times 10^{38} \mathrm{erg\, s^{-1}}} \right)^{-1} \left(\frac{r}{10 \mathrm{pc}} \right). \qquad (10)$$

This suggests that both hadronic and leptonic interactions can be important to explain observed γ-ray photons in ISBs, although L_γ^H dominates for large bubbles.

2.2 X-ray

X-ray emissions depend on the inner structure of the ISB. For a qualitative understanding of X-ray luminosity (L_x), we consider the emission to be due to thermal bremsstrahlung which yields

$$L_x = \int_V dV \left[1.4 \times 10^{-27} Z^2 g_B \, n_e n_i \, T^{1/2} \right]. \qquad (11)$$

We take $Z \approx 1$, $g_B = 1.2$ and $n_e \approx n_i = P_{th}/(k_B T)$ and obtain

$$L_x \approx 3.7 \times 10^5 R^3 T^{-3/2} P_{th}^2$$
$$\sim 3.1 \times 10^{34} \left(\frac{R}{10 \mathrm{pc}} \right)^3 \left(\frac{T}{5 \times 10^7 \mathrm{K}} \right)^{-3/2}$$
$$\times \left(\frac{P_{th}}{10^{-9} \mathrm{cgs}} \right)^2 \mathrm{erg\, s^{-1}}. \qquad (12)$$

In case of CR acceleration, P_{th} will be smaller than in the one-fluid case, which may change L_x. Therefore, the X-ray luminosity is an important diagnostic to identify a CR-dominated bubble.

2.3 Radio

We also wish to estimate the synchrotron emission rate from relativistic electrons. We consider the number density distribution of relativistic electrons to be $n(E) = \kappa_2 E^{-p}$. Note that the normalization constant, κ_2, is not equal to κ_1 of equation (7). Denoting the magnetic field by B, the synchrotron volume emissivity is given by [see equation (8.131) in Longair [2011](#)]

$$j_\nu \simeq 2.3 \times 10^{-25} a(p) B^{(p+1)/2} \kappa_2'$$
$$\times \left(\frac{3.217 \times 10^{17}}{\nu} \right)^{(p-1)/2} \mathrm{J\, s^{-1}\, m^{-3} Hz^{-1}}. \qquad (13)$$

Here $a(p) \simeq 0.45$ for $p = 2.2$ (table 8.2 in Longair [2011](#)), the magnetic field B in Tesla, $\kappa_2 \approx \left[(p-2) \left(m_e c^2 \right)^{p-2} (e_{cr\_e}) \right]$ in J^{p-1} m^{-3}, and κ_2' is obtained from κ_2 after a unit conversion to (GeV)$^{p-1}$ m^{-3}.

---

[1] Here the assumption $\int_V dV = \Delta V$ (i.e. the emission is calculated only in the swept-up shell) may underestimate the γ-ray luminosity because it does not include the ambient contribution; for details see Appendix A.
[2] Depending on CR injection model, W_{sh} may evolve with time, discussed in Section 5.1.1.

[3] Observations of ISBs suggest that the column density is $L \sim 10^{21-22}$ cm^{-2} (e.g. Kim et al. [2003](#); Murphy et al. [2012](#)). For a typical ISB with radius, say $R \sim 10$ pc, number density $\approx L/R \sim 32 - 320$ cm^{-3}.

Table 1. The output from star cluster observations.

[1] Object name	[2] Central source		[3] Bubble	[4] γ-ray		[5] Thermal X-ray			[6] Radio		[7] Ref.
	M_* ($M_\odot$)	L_w (erg s^{-1})	Age (Myr)	R (pc)	E_γ (GeV)	L_γ (erg s^{-1})	T_x (10^6 K)	L_x (erg s^{-1})	ν (GHz)	F_R (Jy)	
30 Doradus	5×10^5	2×10^{39}	2−3	75−100	0.1−20	1.4×10^{37}	4.5	$[4-7] \times 10^{36}$	1.4	56	a, b, c, d, e
Cygnus	3×10^4	3×10^{38}	3−5	≈50	1−100	≈10^{35}	–	$[5-10] \times 10^{35}$	–	–	f, g
NGC 3603	∼10^4	6×10^{38}	1−3	≈30	1−250	≈10^{36}	6.2	$[2-5] \times 10^{35}$	–	–	h, i, j, k
Westerlund 1	5×10^4	∼10^{39}	3−4	≈60	3−300	1.5×10^{34}	6	≲10^{34}	–	–	l, m
Westerlund 2	2×10^4	∼10^{38}	2−3	∼100	>10	6×10^{35}	1,8,36	1.4×10^{34}	–	–	n, o, p

Note: References:: a. Abdo et al. (2010), b. Abramowski et al. (2015), c. Hughes et al. (2007), d. Knödlseder (2013), e. Lopez et al. (2014), f. Ackermann et al. (2011), g. Wright et al. (2010), h. Crowther & Dessart (1998), i. Rosen et al. (2014), j. Yang & Aharonian (2017), k. Harayama, Eisenhauer & Martins (2014), l. Muno et al. (2006), m. Ohm, Hinton & White (2013), n. Rogers & Pittard (2014), o. Yang et al. (2018) and p. Aharonian et al. (2018).

Therefore, the luminosity per unit frequency is

$$
\begin{aligned}
\frac{dL_R}{d\nu} &= \int_v dV j_\nu \\
&\sim 1.4 \times 10^{24} \left(\frac{R}{10\,\mathrm{pc}}\right)^3 \left(\frac{B}{40\,\mu\mathrm{G}}\right)^{1.6} \\
&\times \left(\frac{e_{\mathrm{cr\_e}}}{10^{-10}\mathrm{cgs}}\right) \left(\frac{\nu}{1.4\mathrm{GHz}}\right)^{-0.6} \mathrm{erg\,s^{-1}\,Hz^{-1}}.
\end{aligned}
\tag{14}
$$

In the following sections we use numerical simulations to determine these observables using more realistic analysis.

3 OBSERVATIONS OF ISBS

In Table 1, we show the results from multi-wavelength observation of five massive star clusters. Column 2 shows that the wind mechanical power ranges between $10^{38} \lesssim L_w/(\mathrm{erg\,s^{-1}}) \lesssim 10^{39}$. Column 3 shows the size of the bubble (∼10−100 pc) and their dynamical age (≲5 Myr). The details of γ-ray and X-ray observations are listed in columns 4 and 5, respectively. These indicate that γ-ray luminosity (L_γ) $\lesssim 10^{-2} L_w$ (see also Maurin et al. 2016) and the X-ray luminosity $L_X/L_w \sim 10^{-3}-10^{-2}$. Here the distance for Westerlund 2 is taken as ≈5 kpc (Aharonian et al. 2018; also see Reimer et al. 2007). For all sources, the γ-ray spectral index in 0.1−200 GeV energy band is ≈2.2. Column 6 shows that the radio power from 30 Doradus at 1.4 GHz is $dL_R/d\nu = 4\pi D^2 F_R \sim 1.7 \times 10^{26}$ erg s^{-1} Hz^{-1} (by taking $D \approx 50$ kpc) (Hughes et al. 2007; see also fig. 5 in Foreman et al. 2015).

Note that, out of these objects, in 30 Doradus and Westerlund 2, most of the massive stars are located at the centre. This motivates us to compare our results with them, which is discussed in Section 6.4.

4 SIMULATION SET-UP

We use a modified version of the PLUTO (Mignone et al. 2007) to perform hydrodynamic simulations in the presence of a CR fluid (Gupta et al, in preparation). The following equations are solved:

$$
\frac{\partial \rho}{\partial t} + \nabla . (\rho\,\boldsymbol{v}) = S_\rho
\tag{15}
$$

$$
\frac{\partial}{\partial t}(\rho\,\boldsymbol{v}) + \nabla . (\rho\,\boldsymbol{v} \otimes \boldsymbol{v} + p_{\mathrm{tot}}) = \rho\boldsymbol{g}
\tag{16}
$$

$$
\frac{\partial e_{\mathrm{tot}}}{\partial t} + \nabla . [(e_{\mathrm{tot}} + p_{\mathrm{tot}})\,\boldsymbol{v} + \boldsymbol{F}_{\mathrm{tc}} + \boldsymbol{F}_{\mathrm{crd}}] = \rho\boldsymbol{v}.\boldsymbol{g} + S_e - q_{\mathrm{th}}^{\mathrm{eff}}
\tag{17}
$$

$$
\frac{\partial e_{\mathrm{cr}}}{\partial t} + \nabla . [(e_{\mathrm{cr}} + p_{\mathrm{cr}})\,\boldsymbol{v} + \boldsymbol{F}_{\mathrm{crd}}] = \boldsymbol{v}.\nabla p_{\mathrm{cr}} + S_{\mathrm{cr}} - q_{\mathrm{cr}}.
\tag{18}
$$

Here ρ and $\boldsymbol{v}$ are the mass density and fluid velocity, respectively, $p_{\mathrm{tot}} = p_{\mathrm{th}} + p_{\mathrm{cr}}$ is the sum of thermal and CR pressures, e_{tot} is the sum of kinetic (e_k), thermal (e_{th}) and CR (e_{cr}) energy densities. The adiabatic index for the respective fluids is chosen as $\gamma_{\mathrm{th}} = 5/3$ and $\gamma_{\mathrm{cr}} = 4/3$. We have used HLL Riemann solver, piecewise linear reconstruction and RK2 time stepping. The CFL number is taken as 0.3.

4.1 Ambient medium

The typical size of giant molecular cloud is ∼10−100 pc and masses are ∼$10^4 - 10^6$ $M_\odot$. Detailed observations suggest that the cloud mass and radius follow $M_{\mathrm{cl}} \propto R_{\mathrm{cl}}^2$, i.e. the density profile (ρ) $\propto r^{-1}$ (Solomon et al. 1987; Hughes et al. 2010; Pfalzner et al. 2016). In order to model this, we consider a self-gravitating gas cloud.

The most popular choice for a self-gravitating cloud is an isothermal sphere. A fit for the density profile in this case is given by Natarajan & Lynden-Bell (1997),

$$
\rho(r, r_c) = \rho_c \left[\frac{5}{1 + (r/r_c)^2/10} - \frac{4}{1 + (r/r_c)^2/12}\right].
\tag{19}
$$

Here $r_c = c_s/(4\pi G \rho_c)^{1/2} = [k_B T/(4\pi G \rho_c \mu m_H)]^{1/2} \simeq 2.2\,T_2^{1/2}\,\rho_{c,2}^{-1/2}$ pc is the core radius, T is the temperature, ρ_c is the core density and $\mu = 1.26$ (cold neutral medium). However, this profile does not give $\rho \propto r^{-1}$. We, therefore, relax the isothermal assumption on the global length-scale (∼100 pc) of the cloud. Instead, we add several self-gravitating isothermal clouds and obtain a resultant density profile from

$$
\rho(r) = \sum_{i=1}^n \rho(r, r_c^i),
\tag{20}
$$

where we set the core density and temperature of the clouds as

$$
\rho_c^i = 2^{5-i}\,10\,m_H\,\mathrm{cm}^{-3}\,;\quad T^i = \frac{1600}{2^{5-i}}\,\mathrm{K}
\tag{21}
$$

where $i = 0, 1, 2, ..., 8$ ($n = 8$). This profile provides a dense core (≈$620\,m_H\,\mathrm{cm}^{-3}$) with temperature ≈200 K and a mean surface density $\Sigma \approx 50\,M_\odot\,\mathrm{pc}^{-2}$ (see the comparisons of different ambient profiles in Fig. 1). To maintain hydrostatic equilibrium, we take into account the self-gravity of the individual clouds. The net gravitational acceleration $\boldsymbol{g}$ (see equations 16 and 17) is obtained as

$$
\boldsymbol{g}(r) = \sum_{i=1}^n \frac{\rho(r, r_c^i)}{\rho(r)} \left[\frac{(c_s^i)^2}{\rho(r, r_c^i)} \frac{d}{dr}\rho(r, r_c^i)\right] \hat{r}.
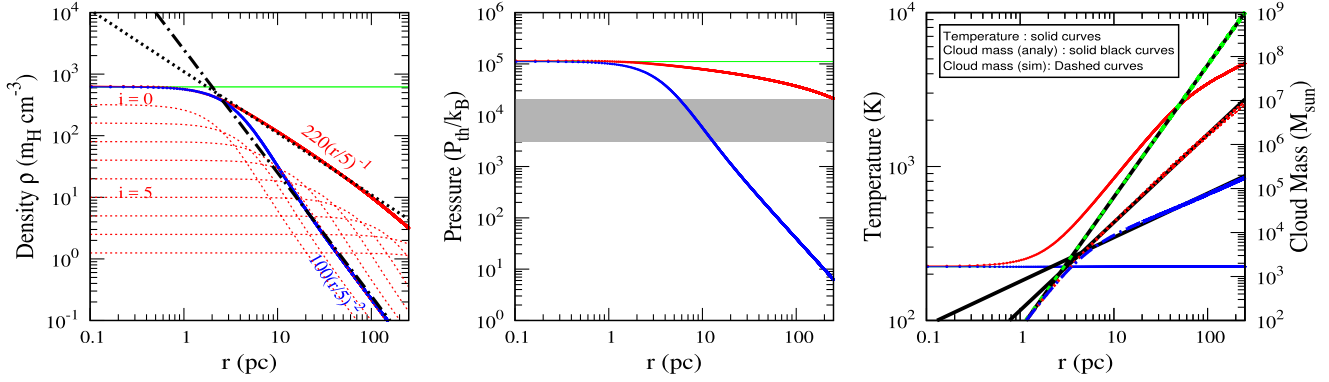\tag{22}
$$

Figure 1. Comparison of three different cloud profiles. Green and blue curves denote a uniform and a non-singular self-gravitating isothermal ambient medium, respectively. Red curves represent the ambient medium used in this work. The grey shaded region in the middle panel shows the average thermal pressure ($P \sim G\Sigma^2$) observed in molecular clouds (Hughes et al. 2010). In the right-most panel, dashed (solid black) curves show the cloud mass for respective profiles obtained numerically (analytically), i.e. for $R_{cl} = 250$ pc, $M_{cl} \simeq 10^9$, 9×10^6 and 1.7×10^5 $M_{\odot}$, respectively.

We find that the ambient profiles are stable for a few hundred Myr.

Note that the cloud profile obtained here is not unique. One can choose a different set of parameters to obtain different ambient density profiles. Furthermore, in a realistic scenario, the ambient medium consists of high-density clumps ($\gtrsim 10^4$ m_H cm^{-3}). Therefore, our ambient profile should be treated as a directionally averaged cloud profile.

4.2 Wind-driving region

For the runs performed in 1D spherical geometry, we choose a spherical region of radius $r_{inj} = 1$ pc around $r = 0$ and set a fine spatial resolution ($\Delta r = 0.05$ pc). This allows us to minimize non-physical cooling losses at the early stages of shock formation [see section 4 in Sharma et al. 2014, also see equation (10) in Gupta et al. 2016]. In our fiducial set-up, we set $\dot{M} = 4 \times 10^{-4}$ $M_{\odot}$ yr^{-1} and $L_w = 5 \times 10^{38}$ erg s^{-1} which have been added uniformly (i.e. $S_{\rho} = \dot{M}/V_{inj}$ and $S_e = L_w/V_{inj}$ where $V_{inj} = 4\pi r_{inj}^3/3$). Therefore, at the sonic point ($r = 1$ pc), the wind velocity is 1414 km s^{-1} which asymptotically approaches $v_w = (2L_w/\dot{M})^{1/2} \approx 2000$ km s^{-1} (Chevalier & Clegg 1985). We discuss the dependence of our results on these parameters in Section 6.1.

To test the reliability of our fiducial 1D model, we perform 3D simulation, particularly to study the effects of distributed stars. For these runs we use Cartesian geometry and distribute a total $N_* = 500$ (assumed) injection points by using a Gaussian random number generator with zero mean value and the standard deviation of 1 pc along x, y, z directions (cf. Fig. 4). The radius of the injection points is taken as $\delta r_{inj} = 0.3$ pc, where mass and energy are added uniformly (similar to 1D). The spatial resolution in the central region, [(x, y, z) $\in (-5, 5)$ pc] which covers all injection points, is set to 0.125 pc.

4.3 CR injection

We use the following two scenarios for CR injection:

(i) Injection in the wind-driving (IWD) region: Internal shocks in the wind-driving region can be an efficient site for CR acceleration. However, it is difficult to spatially resolve them. To investigate this type of acceleration scenario, we use a parameter ϵ_{cr} to denote the fraction of wind energy injected into CRs. The fiducial value is $\epsilon_{cr} = 0.1$.

(ii) Injection at the shock (ISH): In this case, we have injected CRs directly at the resolved shocks (i.e. at forward and reverse shock of the ISB). To identify whether a computation zone is shocked or not, we use the following conditions.

(a) $\nabla \cdot \boldsymbol{v} < 0$,
(b) $\Delta x |\nabla p|/p \geq \delta_{tolerance}$
(c) $\nabla T \cdot \nabla \rho > 0$.

In this work we have taken $\delta_{tolerance} = 1.5$. The last condition helps to exclude spurious oscillations at the contact discontinuity which can be detected as a shock (Pfrommer et al. 2017). We then find the total non-kinetic energy density of the shocked zone (i.e. $e_{th} + e_{cr}$) and redistribute it by a parameter ϵ_{cr}^{ISH} such that the CR pressure fraction of the shocked zone $w = p_{cr}/(p_{th} + p_{cr}) = \epsilon_{cr}^{ISH}/(2 - \epsilon_{cr}^{ISH})$.

Note that the fraction of energy transfer depends on the location of the grid point, which is not necessarily the peak location (density/pressure) of a shock. This may reduce the effective post-shock CR pressure (which determines the CR pressure fraction W_{in}/W_{sh} in the interior/shell) from the injected value (w).

In both injection models, we ensure that CR injection does not add any additional energy in the computational zone. We simply distribute a fraction of the mechanical energy in the form of CRs either in the wind-driving region or at the shocks.

4.4 Microphysics

4.4.1 Cooling losses and heating

Cooling loss of the thermal fluid is taken into account by using a tabulated cooling function for the gas metallicity $Z = 0.4 Z_{\odot}$. To mimic photo-ionization heating from the central radiation field (see fig. 4 in Gupta et al. 2016), we turn off cooling when temperature $T < 10^4$ K.

The cooling loss rate of CR fluid due to the hadronic and Coulomb interactions is taken to be $q_{cr} = 7.5 \times 10^{-16} n_H e_{cr}$ erg s^{-1} cm^{-3} (see section 2.1 in Guo & Oh 2008). The corresponding collisional heating rate of thermal gas is given as $2.6 \times 10^{-16} n_H e_{cr}$ erg s^{-1} cm^{-3}. Therefore, q_{th}^{eff} and q_{cr} in equations (17) and (18) are

$$q_{th}^{eff} = \Lambda_N n_i n_e - 2.6 \times 10^{-16} n_e e_{cr} \text{ erg s}^{-1} \text{ cm}^{-3} \quad (23)$$

$$q_{cr} = 7.5 \times 10^{-16} n_e e_{cr} \text{ erg s}^{-1} \text{ cm}^{-3}. \quad (24)$$

Table 2. Simulation parameters.

Parameter	Fiducial	Range covered
L_w (erg s^{-1})	5×10^{38}	10^{38}–10^{39}
v_w (km s^{-1})	2000	≈ 1000–5000
ϵ_{cr}	0.1	0.01–0.20
w	0.33	0.05–0.54
κ_{cr} (cm^2 s^{-1})	5×10^{26}	5×10^{25}–3×10^{27}
Resolution in 1D (pc)	0.05∗, 0.06	0.03–0.50
Resolution in 3D (pc)	0.125∗, 0.79	–

Note: ∗Resolution in the central region (Section 4.2). We keep the central resolution same for all runs and vary the outer resolution only for 1D runs. The resolution for all 3D runs is fixed.

Note that heating due to CR steaming may affect the thermal fluid more than collisional heating. However, it is not possible to include it in our hydrodynamic set-up. Further, we find that the effect of CR collisional heating is negligible in our set-up. The CR heating can be better studied with the help of MHD simulations.

4.4.2 Thermal conduction and CR diffusion

We assume that both TC and CR diffusion are isotropic. We use TC to have the *Spitzer* value ($6 \times 10^{-7} T^{5/2}$ in CGS) and also assume the saturated TC (see section 4.3 in Gupta et al. 2016). The fiducial value of CR diffusion coefficient is set to $\kappa_{cr} = 5 \times 10^{26}$ cm^2 s^{-1}, unless otherwise mentioned (Gupta et al. 2018). For both cases, we choose STS method (Alexiades, Amiez & Gremaud 1996) to speed up the diffusion module.

5 RESULTS

In this section, we present the results from our fiducial runs (see Table 2). We first discuss 1D simulations (Section 5.1) and then compare them with 3D simulations (Section 5.2).

5.1 1D runs

The structural difference between one-fluid and two-fluid ISBs has been discussed in Gupta et al. (2018) (see their section 4.2). Here we present the time evolution of multi-wavelength luminosities.

5.1.1 γ-ray luminosity

To obtain the γ-ray luminosity, we use equation (3) and display the results in the left-most panel of Fig. 2. The dashed and solid curves represent model with and without TC.

The solid curve (without TC) in this figure shows that the γ-ray luminosity (hereafter displayed by violet curves) in both injection models (denoted by circular symbol: IWD and diamond symbol: ISH) is an increasing function of time. This is expected because, as time evolves, the swept-up mass in the shell increases. We also see that the γ-ray luminosity for IWD model (circular symbols) evolves differently from ISH model (diamond symbols). This can be understood from equation (4) which shows $L_\gamma \propto W_{sh} t_{dyn}^{1/4}$. The parameter W_{sh} is the source of difference between the IWD and ISH models for the following reasons.

For IWD, when the Mach number of the reverse shock becomes $\gtrsim 12$, most of the upstream kinetic energy is converted into CRs (Becker & Kazanas 2001; also see section 4.2 in Gupta et al. 2018).

When TC is off (solid curve), this results in a large increase in CR pressure downstream of the reverse shock after $t_{dyn} \gtrsim 2$ Myr. These CRs diffuse and increase the CR pressure in the shell. Therefore, in the early stages of evolution, W_{sh} increases with time. This is illustrated in the subplot of the same panel. The run with TC (dashed curve) shows a similar result but with an earlier rise than without TC ($t_{dyn} \gtrsim 0.5$ Myr).

On the contrary, for the shock injection scenario (ISH), W_{sh} is fixed. This causes a slower change with time. In this case, L_γ hardly shows any difference between with and without TC (compare the diamond symbols connected by solid and dashed lines).

5.1.2 X-ray luminosity

We use the Mekal plasma model (for gas metallicity $Z = 0.4\,Z_\odot$) to estimate the X-ray luminosity in (≈ 0.5–2) keV energy band and the results are displayed in the middle panel of Fig. 2.

Without TC (solid curves), the X-ray luminosity for all models is $\sim 10^{34}$ erg s^{-1} ($\sim 2 \times 10^{-5} L_w$). To illustrate this, we recall equation (12) which yields

$$\frac{L_x}{\text{erg s}^{-1}} \approx 1.7 \times 10^{37} T_7^{-3/2} \left[\left(\frac{\gamma - 1}{9\gamma - 5} \right)^{5/4} (1 - W_{in})^2 \right]$$

$$\times L_{38}^{5/4} (\rho_{c,220} r_{c,5})^{3/4} t_6^{-1/4} \tag{25}$$

where T and W_{in} denote the volume-averaged temperature and CR pressure fraction inside the bubble, respectively.

Without CRs, for our fiducial parameter $T_7 \approx 5$, equation (25) gives $L_x \approx 2.9 \times 10^{35}$ erg s^{-1} at $t_{dyn} \approx 3$ Myr. However, in the simulation we find $L_x \simeq 1.5 \times 10^{34}$ erg s^{-1}. The difference arises because T is outside of our range of interest (≈ 0.5–2keV) and also because of cooling losses in the bubble (cf. Fig. 6).

The variation of L_x in different models is schematically shown in Fig. 3. For the IWD model, due to an efficient energy transfer from thermal to CR fluid at the reverse shock, the temperature reduces to $T_7 \sim 0.4$ and $(1 - W_{in})^2 \sim 10^{-2}$ (see figs 9 and 10 in Gupta et al. 2018), leading to $L_x \approx 2 \times 10^{34}$ erg s^{-1}. In contrast, L_x in ISH model depends on W_{in} (a larger w corresponds to smaller L_x) (see diamond and pentagon symbols in Fig. 2).

A noticeable difference between IWD and ISH models is found when we include TC, displayed by the dashed curves in the middle panel of Fig. 2. In the absence of CRs, TC reduces the temperature without affecting the thermal pressure of the SW region. This increases L_x (see equation 25 with a smaller T_7). With CR in the IWD model, the X-ray luminosity is $\gtrsim 10$ times smaller than ISH and one-fluid models. This is because of diffusive acceleration at the reverse shock which diminishes the shocked wind temperature and also reduces the effect of TC. For ISH model, L_x depends on W_{in}, and for our choice of $w = 0.33$, L_x can be large ($L_x \gtrsim 10^{-3} L_w$).

5.1.3 Radio

We use equation (13) to model the synchrotron radio emission. Since we do not include magnetic field (B) in our runs, we use two different methods to estimate the magnitude of B.

The first method uses equipartition of magnetic energy with kinetic (ke)/thermal (th)/CR (cr)/total energy (tot). The second method is motivated by observations that suggest that the magnetic field in a cloud depends on density (Valle 1993). Therefore, the magnetic
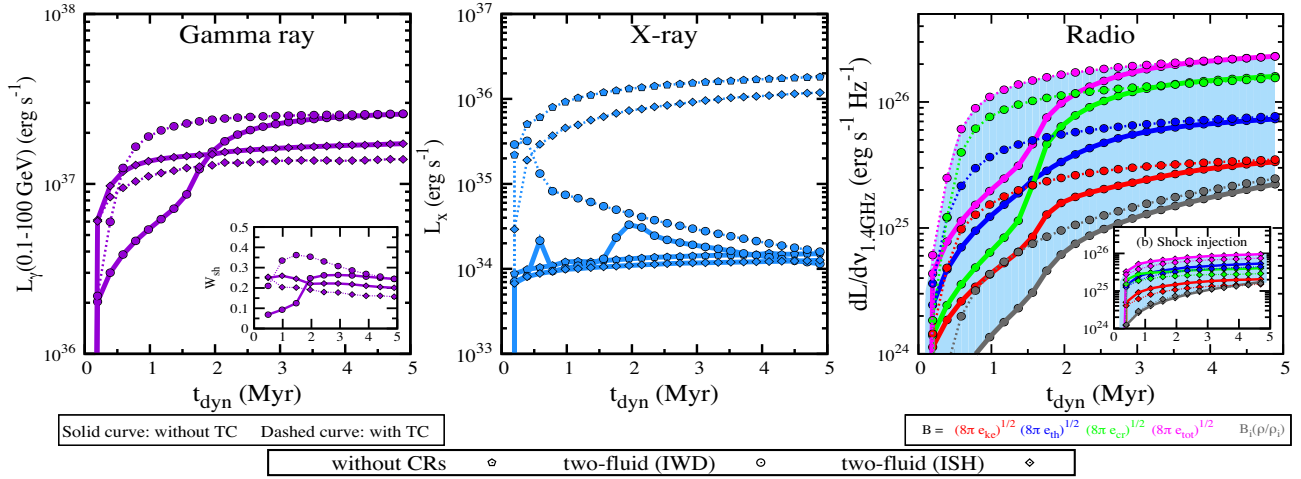
Figure 2. Time evolution of γ-ray (violet), X-ray (blue) and radio luminosities for our fiducial runs (see Table 2). Three different point styles, pentagon and diamond/circle, are used to indicate one-fluid and two-fluid (model: IWD/ISH) ISB, respectively. Dashed/solid line represents runs with/without TC. The sky-blue shaded region in the right-most panel displays the expected radio emission at 1.4 GHz. The figure indicates that luminosities after $\gtrsim 2.5$ Myr do not change significantly.
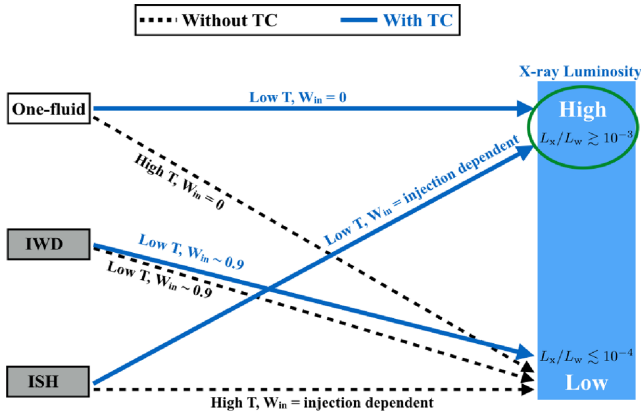

Figure 3. Schematic diagram of L_x ($\propto T^{-3/2}(1 - W_{in})^2$) in different models. In IWD scenario we have only shown the case when the reverse shock is dominated by CRs due to globally smooth solution. In this case it is not possible to produce high L_x. The green circle represents L_x corresponding to observation.

field (B) has been estimated using

$$|\boldsymbol{B}| \approx \begin{cases} \sqrt{8\pi e_x} & \text{where x : ke/th/cr/tot} \\ B_i \, (\rho/\rho_i) \end{cases} \qquad (26)$$

where the subscript 'i' stands for the initial ambient value. For simplicity, we assume $B_i = 10\,\mu G$ to be uniform. Due to ambiguity in magnetic field, we have five degenerate values of L_R ($= \nu dL_\nu/d\nu$), at a given time. The result is shown by different colours in the right-most panel of Fig. 2. Here, we use the same symbols (line styles) to represent IWD and ISH (with/without TC) models.

For IWD model, $L_{1.4GHz}$ is consistent with the analytical estimates (equation 14). The subplot (b) for ISH model shows that the results depend weakly on time. The difference between IWD and ISH models stems for the fact that the fractions W_{in} and W_{sh}, which determine the CR electron energy density (e_{cr_e}), evolve differently in these two models. For details see Sections 5.1.1 and 5.1.2.

The luminosities in all bands show a weak time dependence after ≈ 2.5 Myr. This allows us to compare with observations and explore

the parameter dependence without invoking a particular epoch (cf. Section 6).

5.2 3D runs

5.2.1 Structure and dynamics

To present a more realistic scenario, we perform 3D simulations with the same fiducial parameters (see Table 2). In these runs, mass and energy are injected in a distributed manner. Fig. 4 displays the injection points where the horizontal colour palette represents the z coordinates of those points. The vertical colour palette displays the density snapshot in the $z = 0$ plane at $t_{dyn} = 0.05$ Myr. This
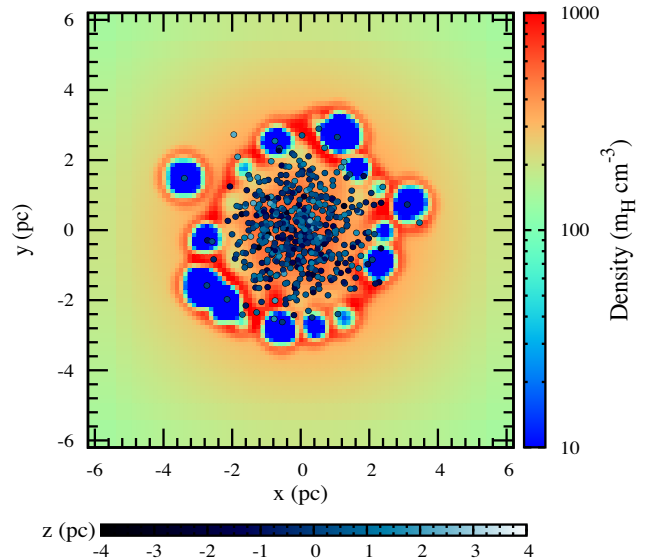

Figure 4. Distributed injection in 3D. The horizontal colour palette displays z-coordinate of the injection points (darker points are in the back and brighter points in front). The vertical colour palette displays the snap shot of density profile in $z = 0$ plane at 0.05 Myr. The figure represents the early stage of bubble formation.
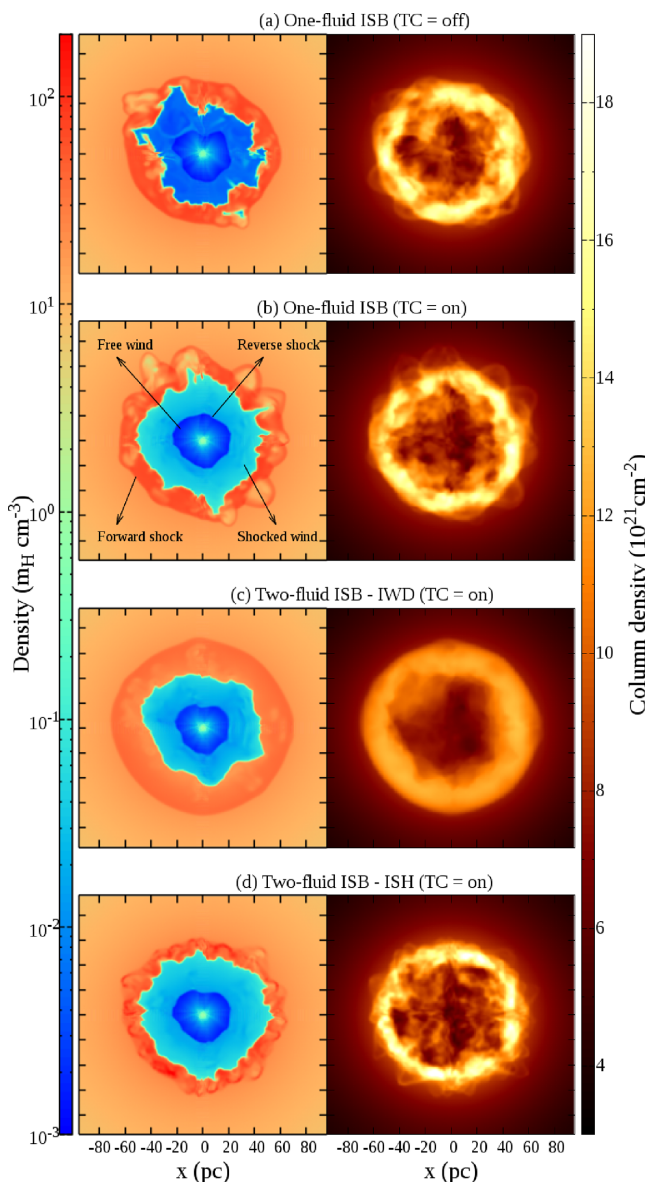
Figure 5. The comparison of density profile at $z = 0$ plane (left panel) and the column density along the z-axis (right panel) at 2.5 Myr. The left panels clearly indicate the four distinct regions of the ISB. The right panels show that information of the internal structure is apparently lost due to projection effect.

shows that individual bubbles have started to merge at this epoch. At a later time ($t_{dyn} \gtrsim 0.5$ Myr), the structure appears as an ISB, as shown in Fig. 5.

The left panel of Fig. 5 shows the snapshot of density profile at $z = 0$ plane for different models. The cumulative effect of all injection points produces a free wind profile followed by a reverse shock, shocked wind and forward shock. Therefore, the structure is very similar[4] to that of a classical ISB.

The size of the bubble carries useful information, e.g. the mass of the shell, the volume of X-ray cavity. Because of the distributed nature of injection points in 3D runs, the size evolution may be

---

[4]It is important to note that the coherent reverse shock may be destroyed if energy is injected via exploding supernovae rather than our smooth stellar winds (see Sharma et al. 2014; Yadav et al. 2017).
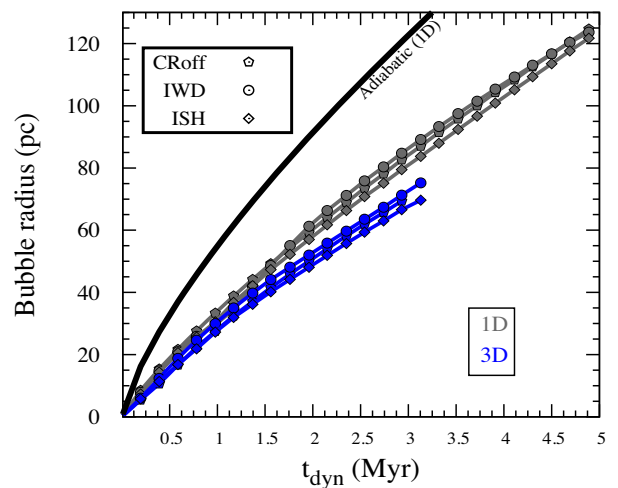

Figure 6. Evolution of bubble radius in 1D and 3D. The comparisons of solid black curve (which stands for a one-fluid adiabatic run i.e. cooling and CRs both are not included) with other curves show that cooling losses have reduced the bubble size. Blue and grey curves (where micro-physics are included; Section 4.4) show that the radius in 3D is smaller than 1D. The comparison of different symbols (having the same colour) indicates that the dynamical impact of CRs is negligible.

different. We show the comparison of 1D (grey curves) and 3D (blue curves) runs in Fig. 6. For both geometries (i.e. spherical and Cartesian), we first estimate the swept-up mass (M_{sh}) and then we obtain the average shell radius by using:

$$R \approx \left[\frac{3-s}{4\pi \rho_c r_c^s} M_{sh} \right]^{1/(3-s)} \tag{27}$$

where $\rho_c = 220 \, m_H \, \text{cm}^{-3}$, $r_c = 5$ pc and $s = 1$ (see Fig. 1). From this figure we find that the radius of the bubble in 3D runs is *smaller* compared to 1D runs. Therefore, the 3D runs are expected to show a *lower* luminosity. Otherwise, the different CR injection models do not show significant change from the one-fluid bubble. Therefore, the dynamical impact of CRs in ISBs may not be important.

5.2.2 Time evolution of luminosities

Following the methods described in Sections 5.1.1, 5.1.2 and 5.1.3, we estimate L_γ, L_x and L_R for our 3D runs. For γ-ray, we compute both hadronic and leptonic components.

In Fig. 7, the solid curves displaying L_γ due to hadronic interaction show a similar time dependence as in 1D. The CR pressure fraction (see subplot) for the models IWD and ISH are $W_{sh} \approx 0.25$ and $W_{sh} \approx 0.17$, respectively. The luminosity is somewhat lower than the 1D cases. This is because the size of the bubble is smaller than in 1D model[5] (Fig. 6). The dashed curves show that inverse Compton scattering is subdominant. The lower panels display the γ-ray surface brightness map (SB_γ). SB_γ due to hadronic and leptonic interactions are obtained from

$$\frac{SB_\gamma}{\text{erg s}^{-1} \, \text{cm}^{-2}} = \begin{cases} \int_{-L}^{+L} dz \left[1.1 \times 10^{-16} \, n_N \, e_{cr} \right] \\ \int_{-L}^{+L} dz \left[172 \times 10^{-16} \left(\frac{r}{10\text{pc}} \right)^{-2} e_{cr} \right], \end{cases} \tag{28}$$

---

[5]Moreover, due to a smaller box size ($2|L|$, spanning from -100 to 100 pc), the ambient contribution is not completely captured in our analysis
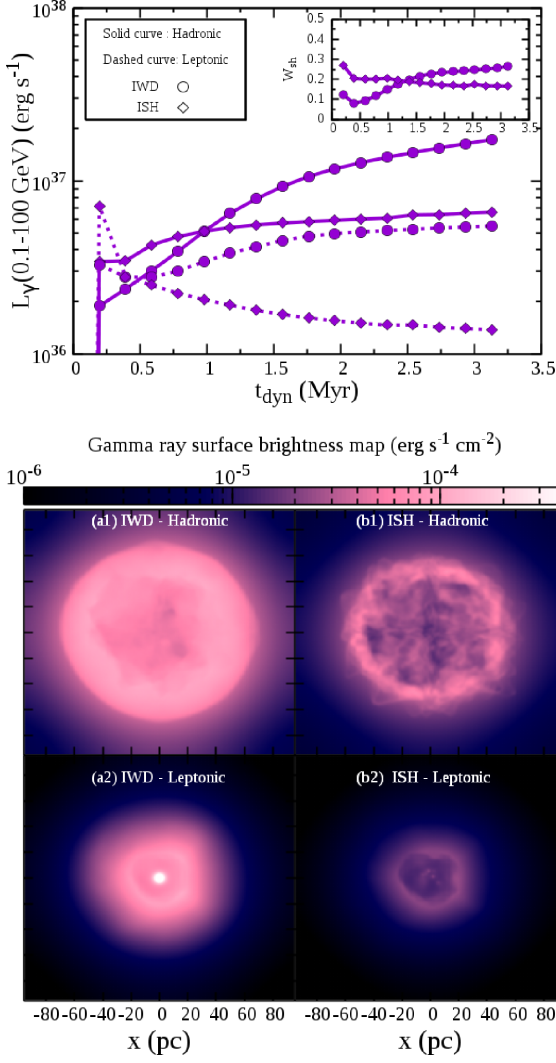
Figure 7. Top panel: Time evolution of L_γ in 3D runs (with TC). The comparison of dashed curves with solid curves for a same symbol (circular: IWD and diamond: ISH) indicates that the inverse Compton scattering is subdominant compared to hadronic interaction (consistent with equation 10). The subplot displays the CR pressure fraction in the shell. Bottom panel: The γ-ray surface brightness map along z direction (equation 28) at 2.5 Myr.

respectively (see equations 3 and 9). The hadronic γ-ray maps (panels a1 and b1) indicate that central region of the bubble is not bright in γ-ray. In contrast, for leptonic γ-ray model (panels a2 and b2), the stellar radiation field increases the γ-ray brightness in central region. This can be a diagnostic to distinguish between the hadronic and leptonic models.

Fig. 8 for X-ray luminosity shows that the one-fluid with TC model[6] (pentagon symbol) $L_x \approx 1.7 \times 10^{35}$ erg s^{-1} at $t_{dyn} \gtrsim 2$ Myr. Removal of TC makes it dimmer by a factor of ~ 10. For ISH model, L_x approaches $\approx 1.5 \times 10^{35}$ erg s^{-1}, for our choice of small w. L_x for the IWD model is close (difference $\lesssim 3$) to one-fluid ISB without TC. In other words, the presence of CRs can mimic the absence of TC.

The projection maps (obtained similarly as the γ-ray map) for respective models are shown in the bottom panels. The maps clearly
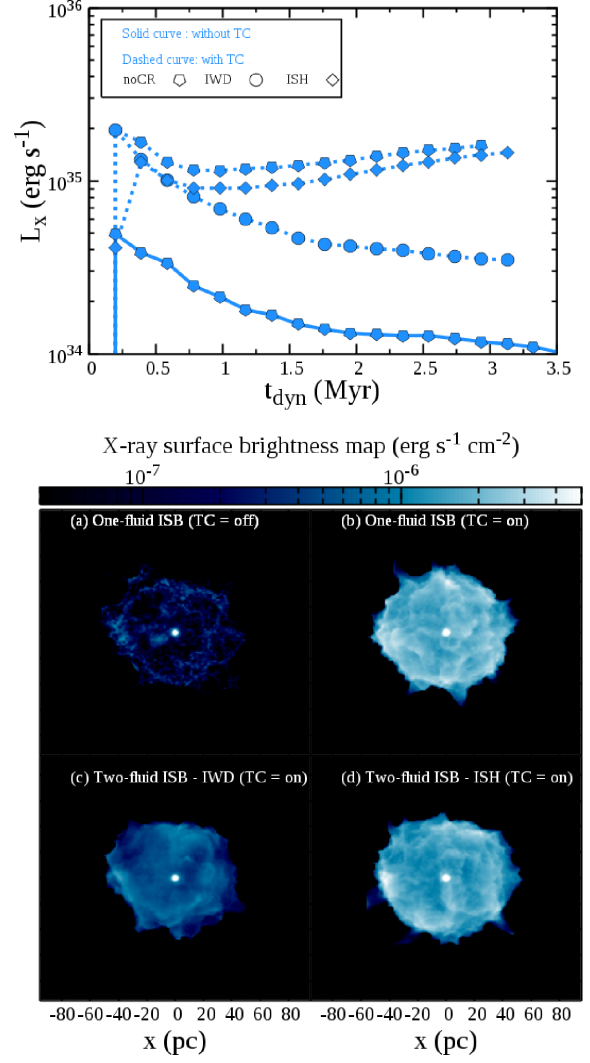
Figure 8. Top panel: Time evolution of L_x in 3D. The luminosity in IWD model is smaller than ISH model by a factor of ≈ 5. Bottom panel: X-ray ($\approx 0.5-2$keV) surface brightness map projected on x-y plane at 2.5 Myr.
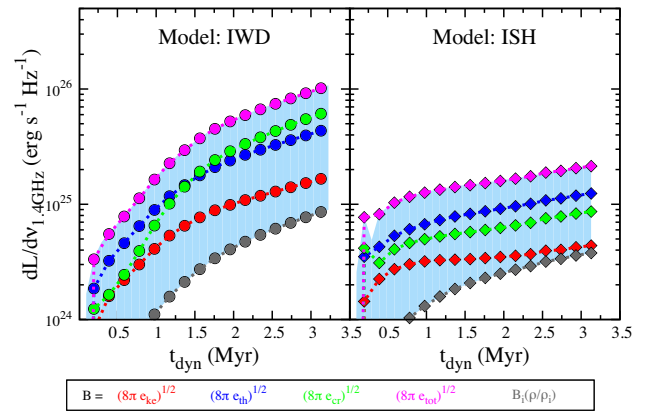

Figure 9. Time evolution of radio luminosity per unit frequency for two different CR injection models in 3D runs.

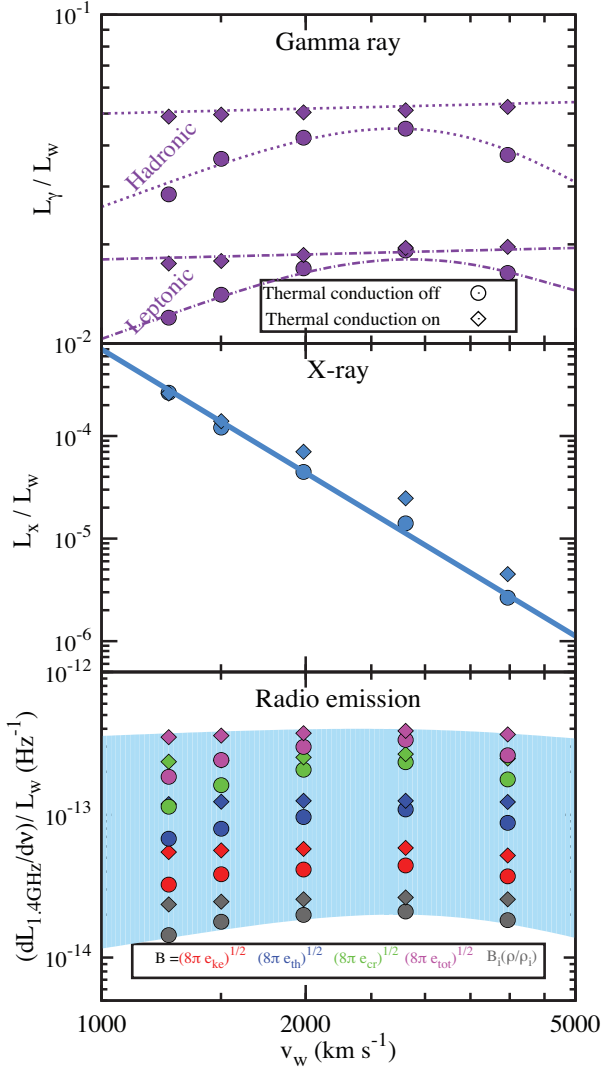[6]L_x is smaller than that of 1D simulation. For details see Appendix B.

Figure 10. Dependence of γ-ray, X-ray and radio luminosities (normalized w.r.t L_w) on the wind velocity (v_w) at 3 Myr for IWD model. The diamond/circle symbols stand for with/without TC run. The sky-blue shaded region shows the expected range for radio luminosity.

show that for one-fluid model, TC can increase X-ray surface brightness (as illustrated in Fig. 3). Consider now the effect of CRs. If the wind-driving region (IWD) is the main site for CR acceleration, the X-ray surface brightness is dimmer than shock injection model (ISH). Therefore, the surface brightness profile is an important diagnostic to identify CR acceleration site. Later, we will show that observations prefer the ISH (brighter) model.

Fig. 9, which displays the radio luminosity per unit frequency at 1.4 GHz, follows a similar evolution as in 1D runs. From this section, we conclude that the 3D results qualitatively agree with 1D runs.

6 DISCUSSIONS

In the previous section, we have studied the time evolution of γ-ray, X-ray and radio luminosities, and the difference between 1D and 3D models. Here we explore the dependence of our results on different parameters using 1D runs.
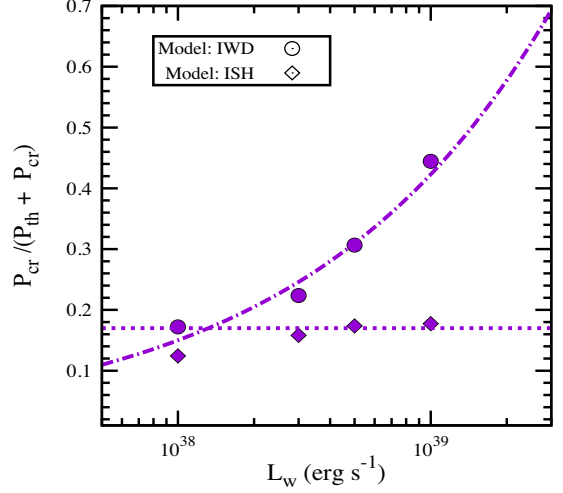

Figure 11. The ratio of volume-averaged CR pressure to total pressure in the swept-up ISM as a function of wind luminosity at 3 Myr. We see a similar dependence for $t_{dyn} \sim 1-5$ Myr.

6.1 Wind velocity

Although the wind velocity ($\approx (2L_w/\dot{M})^{1/2}$) is a critical parameter, it does not have a well-defined prescription. Fig. 10 shows the dependence of our results (L_γ, L_x and L_R in top, middle and bottom panels) on this parameter for the IWD case.

The top panel of Fig. 10 displays L_γ. Two different line-styles (dotted and dash–dotted), which represent L_γ due to hadronic and leptonic interactions, indicate that the hadronic interaction dominates over inverse Compton scattering (Section 2.1.2). When TC is off (see circles) and the wind velocity (v_w) is varied from 1000 to 4000 km s^{-1}, the γ-ray luminosity changes by a factor of ~ 2. In contrast, for the models with TC (the diamond symbols), L_γ is almost independent of v_w (the violet curve).

The middle panel displaying the X-ray luminosity shows a significant dependence on v_w. A small v_w indicates a large $\dot{M}$, correspondingly a large density, and it results in a high L_x. However, if v_w is too small ($v_w \lesssim 1200$ km s^{-1} and $\dot{M} \gtrsim 10^{-3} M_\odot$ yr^{-1}) then the shocked-wind region radiates so efficiently that it disappears and the X-ray emission is quenched ($L_x/L_w \ll 10^{-6}$).

The bottom panel shows the synchrotron emission at 1.4 GHz. This panel shows a moderate (within a factor of ≈ 2) dependence on v_w.

In ISH model, all luminosities (not displayed) show a similar dependence on v_w when TC is off. However, in runs with TC, the X-ray luminosity is $\gtrsim 10^{-3} L_w$, which is significantly higher than that in IWD model.

6.2 Star cluster mass and CR parameters

Here we explore the dependence on three important parameters. The first one is the mechanical luminosity (L_w) which depends on cluster mass. The other two parameters are the CR injection fraction and diffusion coefficient. In all our runs discussed in this section TC is included.

6.2.1 Non-thermal pressure in the shell

We have estimated the volume-averaged CR and thermal pressure in the shell for four different values of L_w, where the other parameters
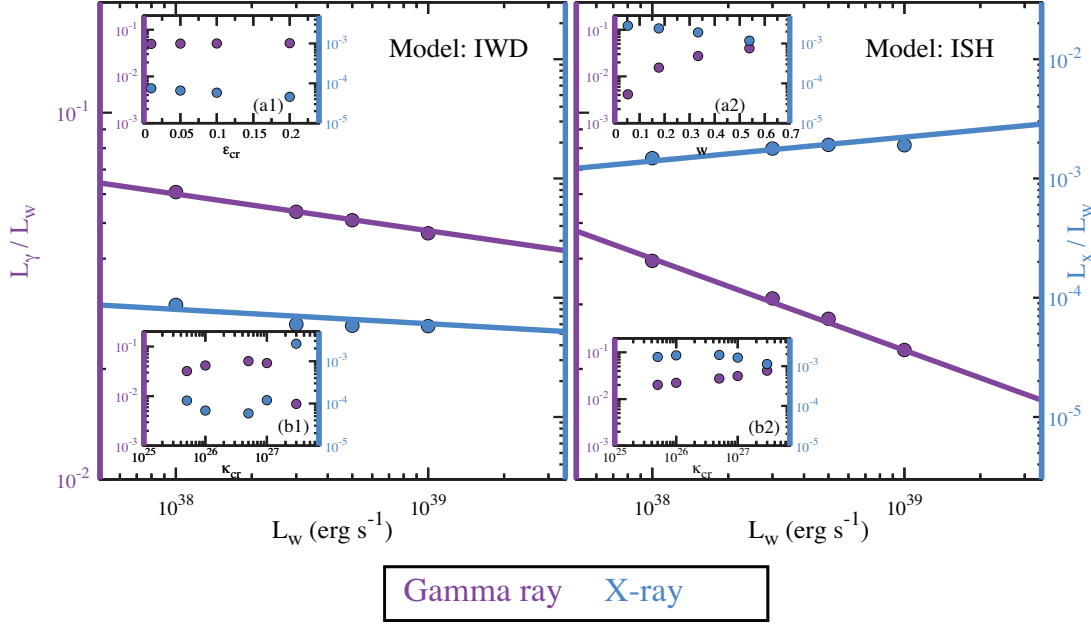
Figure 12. Parametric study of γ-ray (violet) and X-ray (blue) luminosities. The violet and blue coloured vertical axes display L_γ and L_x, respectively. The subplot (a1)/(a2) displays the dependence of results on the CR injection fraction (ϵ_{cr} or w), and (b1)/(b2) shows the dependence on the CR diffusion coefficient. The subplot (a1) shows that L_γ and L_x do not depend on the injection fraction. The subplot (b1), (a2) and (b2) indicate an anti-correlation of L_γ with L_x.
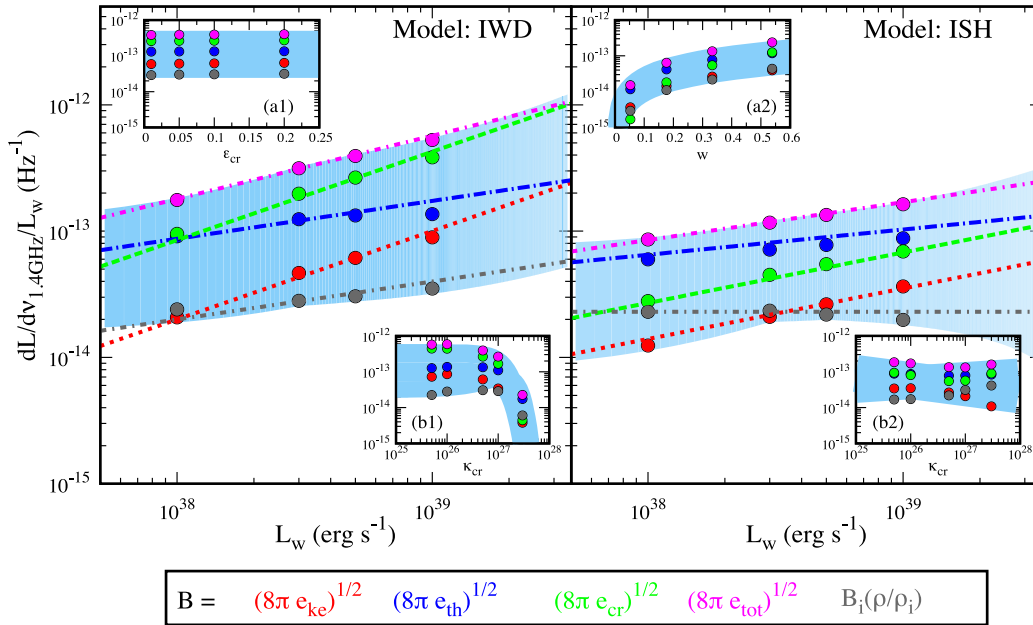

Figure 13. Parametric study of the synchrotron radio luminosity per frequency ($dL/d\nu$) at 1.4 GHz. Due to ambiguity in magnetic field (B), $dL/d\nu$ is spread over the sky-blue shaded region. In both panels, L_R ($= \nu dL/d\nu$) increases with L_w. The subplots (a1) and (b2) display that L_R does not depend on ϵ_{cr} and κ_{cr}. The subplot (b1) (and (a2)) shows that L_R decreases (increases) with κ_{cr} (w).

are kept identical to the fiducial run (Table 2). The dotted straight line in Fig. 11 verifies that the CR pressure fraction, i.e. $W_{sh} =$

$P_{cr}/(P_{cr} + P_{th}) \approx 0.17$ is fixed in ISH. In contrast, the dash-dotted curve (IWD) shows that the CR pressure fraction increases as $W_{sh} \propto$

$L_{\rm w}^{0.45}$. This indicates that if the wind-driving region is an efficient site for CR acceleration (IWD) then for massive star clusters, CR pressure in the shell can be comparable to or larger than thermal pressure.

6.2.2 γ-ray, X-ray and Radio

In Figs 12 and 13, we display the variation of L_{γ}, $L_{\rm x}$ and $L_{\rm R}$ on all three parameters ($L_{\rm w}$, $w/\epsilon_{\rm cr}$ and $\kappa_{\rm cr}$). The main plot shows the dependence on $L_{\rm w}$; the subplots (a) and (b) show the dependence on CR injection fraction ($\epsilon_{\rm cr}/w$) and diffusion coefficient ($\kappa_{\rm cr}$) respectively.

(i) IWD (left panels of Figs 12 and 13): We find that $L_{\gamma} \propto L_{\rm w}^{0.9}$, $L_{\rm x} \propto L_{\rm w}^{0.9}$ and $L_{\rm R} \propto \nu dL_{\rm R}/d\nu \propto L_{\rm w}^{1.3-1.7}$. The small variation of L_{γ} can be understood from equation (4) which yields $L_{\gamma} \propto W_{\rm sh} L_{\rm w}^{3/4}$. Since $W_{\rm sh} \propto L_{\rm w}^{0.45}$ (see Fig. 11), we expect $L_{\gamma} \propto L_{\rm w}^{1.2}$. However, in simulation we get a weaker dependence because for a low $L_{\rm w}$ (i.e. a smaller bubble and high-density ambient medium), the ambient contribution enhances L_{γ}. Important point to note is that $L_{\rm x} < L_{\rm w}/10^4$ (blue). The subplot (a1) in both figures indicates that all luminosities are insensitive to the CR injection fraction ($\epsilon_{\rm cr}$). The subplot (b1) shows that $L_{\rm x}$ and L_{γ} are anti-correlated when $\kappa_{\rm cr}$ is varied $5 \times 10^{25} \lesssim \kappa_{\rm cr}/{\rm cm}^2\,{\rm s}^{-1} \lesssim 3 \times 10^{27}$. This is because a sufficiently large (or sufficiently small) $\kappa_{\rm cr}$ diminishes the efficiency of CR re-acceleration (for details, see section 4.2 in Gupta et al. 2018) which increases $L_{\rm x}$ but decreases L_{γ}. We conclude that L_{γ} can be as large as ≈ 5 per cent of $L_{\rm w}$ only when $10^{26} \lesssim \kappa_{\rm cr}/{\rm cm}^2\,{\rm s}^{-1} \lesssim 10^{27}$.

(ii) ISH (right panels of Figs 12 and 13): Figures show that $L_{\gamma} \propto L_{\rm w}^{0.75}$, $L_{\rm x} \propto L_{\rm w}^{1.2}$ and $dL_{\rm R}/d\nu \propto L_{\rm w}^{1-1.4}$. The dependence of L_{γ} and $L_{\rm x}$ is therefore consistent with equations (4) and (25). The subplot (a2) confirms that L_{γ}, $L_{\rm x}$ and $L_{\rm R}$ change almost linearly with the injection fraction (w). The subplot (b2) shows that L_{γ} increases with $\kappa_{\rm cr}$. This is because we have used a fixed w irrespective of $\kappa_{\rm cr}$. A larger CR diffusion enhances the ambient contribution and hence it increases L_{γ}. In contrast, $L_{\rm x}$ is changed only by a factor of $\lesssim 2$ because in this model the interior of the ISB does not depend on $\kappa_{\rm cr}$.

6.3 Thermal versus non-thermal radio

The radio emission discussed in previous sections is based on synchrotron emission from non-thermal (relativistic) electrons. However, we know that young star clusters generate UV photons which can ionize gas and give rise to thermal radio emission. To compare it with non-thermal radio luminosity, we estimate thermal bremsstrahlung emission rate at 1.4 GHz by using

$$\frac{dL}{d\nu}\big|_{\rm ff} = \int_V dV \left[6.8 \times 10^{-38} n_{\rm i}\, n_{\rm e}\, Z^2 T^{-1/2} \exp\left(-\frac{h\nu}{k_{\rm B}T}\right) \right] \quad (29)$$

in ${\rm erg\,s}^{-1}\,{\rm Hz}^{-1}$ (see equation 5.14b in Rybicki & Lightman 1979). Here we take $n_{\rm i} = \rho/(\mu_{\rm i} m_{\rm H})$, $n_{\rm e} = \rho/(\mu_{\rm e} m_{\rm H})$, $Z = 1$ and $g_{\rm ff} = 1$. For a completely ionized gas ($T \gtrsim 8000$ K), the mean mass per ion and electron are taken to be $\mu_{\rm i} = 1.27$, $\mu_{\rm i} = 1.17$ (gas metallicity $0.4 Z_{\odot}$).

It is important to note that in a realistic scenario, $\mu_{\rm e}$ depends on gas temperature which further depends on the photo-ionization heating (see e.g. section 4.5 in Gupta et al. 2016). For an order of magnitude estimate, we use a simple prescription given in appendix A of Gupta et al. (2016) to estimate $\mu_{\rm e}$.
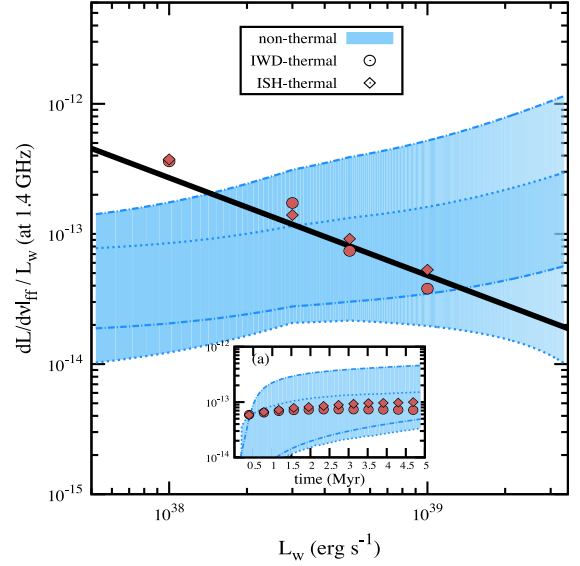

Figure 14. Thermal radio emission rate at 1.4 GHz. The sky-blue shaded regions bounded by dash–dotted and dotted curves represent the corresponding range of non-thermal radio for the models IWD and ISH, respectively (see Fig. 13). The subplot (a) displays the time evolution $dL/d\nu|_{\rm ff}/L_{\rm w}$ for our fiducial run (i.e. $L_{\rm w} = 5 \times 10^{38}\,{\rm erg\,s}^{-1}$).

To find an analytical expression for the thermal radio luminosity, we assume that only the swept-up shell contributes to it, i.e. $\int_V dV \approx \Delta V$. For the density profile we have considered, equation (29) yields to

$$\frac{dL}{d\nu}\big|_{\rm ff} = 4 \times 10^{24} \left(\frac{R}{10{\rm pc}}\right) \left(\frac{\rho_{\rm c}}{220 m_{\rm H}{\rm cm}^{-3}}\right)^2 \left(\frac{r_{\rm c}}{5{\rm pc}}\right)^2 \quad (30)$$

in ${\rm erg\,s}^{-1}\,{\rm Hz}^{-1}$. A comparison of equations (14) and (30) indicates that thermal radio is comparable to non-thermal radio emission. Thermal radio dominants over non-thermal radio for a smaller bubble, and also for a higher frequency (compare R or ν dependence of equations 14 and 29/30). It is worth mentioning that radio emission can also arise from ambient region which may increase the net $dL/d\nu|_{\rm ff}$. To obtain a more accurate estimate, we calculate the emission rate from our simulations by using equation (29) (integration is performed up to $r = 250$ pc).

Fig. 14 shows $dL/d\nu|_{\rm ff}$ (normalized w.r.t $L_{\rm w}$) as a function of $L_{\rm w}$ at 3 Myr. As expected from equation (30), at $t_{\rm dyn} = 3$ Myr, $dL/d\nu|_{\rm ff} \approx 2.7 \times 10^{25} L_{w,38}^{1/4}\,{\rm erg\,s}^{-1}\,{\rm Hz}^{-1}$ (using $R \approx 0.6[L_w t^3/(\rho_c r_c)]^{1/4}$) which is shown by the solid line. Note that, despite being a smaller bubble size (see Fig. 6), due to ambient contribution, the numerical results do not differ much from the predicted value of equation (30). The subplot (a) shows the time evolution of $dL/d\nu|_{\rm ff}$ for our fiducial run. The sky-blue shaded regions, bounded by dash-dotted (IWD) and dotted (ISH) curves, represent the corresponding range for non-thermal radio emission (displayed Fig. 13). Therefore, in young star clusters, the non-thermal and thermal radio luminosities at 1.4 GHz are almost comparable.

6.4 Comparison with observation

We are now at a stage to compare with observation. Young star clusters ($\lesssim 3.5$ Myr) are powered mainly by stellar winds (Leitherer et al. 1999, see also fig. 1 in Gupta et al. 2016). If stars are distributed in a compact region then a coherent reverse (termination) shock is

expected to form. Even if there are supernovae and massive transient winds from within the star cluster, we do not expect the scenario to change significantly as long as the energy deposited by the smooth winds dominates.

For 30 Doradus, most of the massive stars are located at the central few pc region (e.g. Massey & Hunter 1998; Selman et al. 1999). Table 1 shows that for 30 Doradus $L_\gamma/L_w \sim 10^{-2}$, $L_x/L_w \sim 2 \times 10^{-3}$ and $(dL_R/d\nu)/L_w \sim 8 \times 10^{-14}\,\text{Hz}^{-1}$. This suggests that the forward and reverse shock injection model (ISH) is the most preferable one (see the right panels in Figs 12 and 13 with $L_w \approx 2 \times 10^{39}\,\text{erg s}^{-1}$). We can also put an upper limit of $\lesssim 0.2$ on the ratio of CR pressure to thermal pressure in the photo-ionized shell (Fig. 11). Moreover, our results also suggest that TC is indeed required to explain L_x, because without it $L_x/L_w \lesssim 10^{-4}$.

Another star cluster, Westerlund 2, has a compactness similar to 30 Doradus in terms of stellar distribution. From our model, we expect to have large L_γ and small L_x. Recent observations show that $L_\gamma/L_w \sim 6 \times 10^{-3}$ and $L_x/L_w \sim 1.4 \times 10^{-4}$ (see Table 1). Moreover, radio observation indicates the presence of non-thermal emission (Benaglia et al. 2013). This supports that compact star clusters can efficiently accelerate CRs. This is consistent with a recent finding of Aharonian et al. (2018).

For other objects listed in Table 1, $L_\gamma/L_w \lesssim 10^{-3}$. The reason could be a low-density ISM or the stellar distribution is not compact. However, their structures are quite irregular, and our simplified model may not be suitable for a meaningful comparison.

7 CONCLUSIONS

We have presented the detailed diagnostics of the γ-ray, X-ray and radio luminosities to understand the effects of CR in a young star cluster. This work is an extension of Gupta et al. (2018) which demonstrated the two-fluid model of an ISB. Our key results are as follows:

(i) Ambient medium: We have modelled an ambient density profile (mean surface density $\sim 50\,M_\odot\,\text{pc}^{-2}$) that follows $M_{cl} \propto R_{cl}^2$ (Section 4.1, Fig. 1). This profile makes the resulting γ-ray luminosity weakly dependent on time (Section 2.1.1), and allows a convenient comparison with observation.

(ii) ISB profiles: The structure of ISB plays a crucial role in the comparison with observations. We have focused on the early phases of bubble evolution ($\lesssim 4$ Myr; i.e. ISB is driven by the stellar wind, not supernovae), and show that 3D structure is consistent with 1D runs (Fig. 5).

(iii) Dynamical effects of CRs: We compare bubble radius between with and without CR models by considering two different CR injection scenarios (models: IWD and ISH, Section 4.3). Our models do not show a noticeable difference in the bubble radius (Fig. 6).

(iv) Multi-wavelength luminosities: We find that if central wind-driving (IWD) region accelerates CRs then γ-ray luminosity (L_γ) can reach ≈ 5 per cent of the wind mechanical power (L_w) when the reverse shock is CR dominated. In this scenario, L_γ is almost independent of the CR injection fraction (Fig. 12) and the X-ray luminosity $\lesssim L_w/10^4$. If the forward/reverse shock (ISH) of an ISB is the CR injection site, then the γ-ray luminosity is directly proportional to injection fraction (w) and X-ray luminosity ($\gtrsim L_w/10^3$) is reduced by a factor of $\sim (1-w)^2$ from one-fluid model (Fig. 12). We also show the expected range for the radio emission at 1.4 GHz (Fig. 13).

(v) Comparison with observation: We compare our models with two well-observed star clusters, 30 Doradus and Westerlund 2. We find that the CR injection at the reverse and forward shocks (ISH model) can explain multi-wavelength observations.

Therefore, we suggest that the comparison of the γ-ray, X-ray and radio luminosities with the wind mechanical power will help to know the details of CR acceleration in star clusters.

REFERENCES

Abdo A. A. et al., 2010, A&A, 512, A7
Abramowski A. et al., 2015, Science, 347, 406
Ackermann M. et al., 2011, Science, 334, 1103
Aharonian F. A., Atoyan A. M., 1996, A&A, 309, 917
Aharonian F., Yang R.-z., de Oña Wilhelmi E., 2018, preprint (arXiv:1804.02331)
Alexiades V., Amiez G., Gremaud P.-A., 1996, Com. Num. Meth. Eng., 12, 31
Becker P. A., Kazanas D., 2001, ApJ, 546, 429
Benaglia P. et al., 2013, A&A, 559, 31
Booth C. M., Agertz O., Kravtsov A. V., Gnedin N. Y., 2013, ApJ, 777, L16
Bykov A. M., 2014, A&AR, 22, 77
Chevalier R. A., 1983, ApJ, 272, 765
Chevalier R. A., Clegg A. W., 1985, Nature, 317, 44
Chu Y.-H., Guerrero M. A., Gruendl R. A., Garcia-Segura G., Wendker H. J., 2003, ApJ, 599, 1189
Crowther P. A., Dessart L., 1998, MNRAS, 296, 622
Dale J. E., Ercolano B., Bonnell I. A., 2013, MNRAS, 430, 234
de Grijs R., 2010, Phil. Trans. R. Soc. A, 368, 693
Dermer C. D., 1986, A&A, 157, 223
Drury L. O'C., Falle S. A. E. G., 1986, MNRAS, 223, 353
Drury L. O'C., Völk J. H., 1981, ApJ, 248, 344
Foreman G. et al., 2015, ApJ, 808, 44
Guo F., Oh S. P., 2008, MNRAS, 384, 251
Gupta S., Nath B. B., Sharma P., Shchekinov Y., 2016, MNRAS, 462, 4532
Gupta S., Nath B. B., Sharma P., Eichler D., 2018, MNRAS, 473, 1537
Harayama Y., Eisenhauer F., Martins F., 2014, ApJ, 675, 1319
Harper-Clark E., Murray N., 2009, ApJ, 693, 1696
Hughes A., Staveley-Smith L., Kim S., Wolleben M., Filipovic M., 2007, MNRAS, 382, 543
Hughes A. et al., 2010, MNRAS, 406, 2065
Kim S. et al., 2003, ApJS, 148, 473
Kim C.-G., Ostriker E. C., 2015, ApJ, 802, 99
Knödlseder J., 2013, ASSP, 34, 169
Krause M. et al., 2013, A&A, 550, 49
Leitherer C. et al., 1999, ApJS, 123, 3
Longair M. S., 2011, High Energy Astrophysics, 3rd edn. Cambridge Univ. Press, Cambridge, NY
Longmore S. N. et al., 2014, Protostars and Planets VI, 914, 291
Lopez L. A., Krumholz M. R., Bolatto A. D., Prochaska J. X., Ramirez-Ruiz E., Castro D., 2014, ApJ, 795, 121
Mannheim K., Schlickeiser R., 1994, A&A, 286, 983
Martizzi D., Faucher-Giguére C.-A., Quataert E., 2015, MNRAS, 450, 504
Massey P., Hunter D. A., 1998, ApJ, 493, 180
Maurin G. et al., 2016, A&A, 591, 71

Mignone A. . et al., 2007, ApJS, 170, 228

Muno M. P. et al., 2006, ApJ, 650, 203

Murphy E. J., Porter T. A., Moskalenko I. V., Helou G., Strong A. W., 2012, ApJ, 750, 126

Natarajan P., Lynden-Bell D., 1997, MNRAS, 286, 268

Nath B. B., Shchekinov Y., 2013, ApJ, 777, L1

Ohm S., Hinton J. A., White R., 2013, MNRAS, 434, 2289

Persic M., Rephaeli Y., 2015 , in Cosmic-Ray Proton to Electron Ratios . World Scientific Publishing, p. 1036

Pfalzner S. et al., 2016, A&A, 586, 68

Pfrommer C., Enßlin T. A., 2004, A&A, 413, 17

Pfrommer C. et al., 2017, MNRAS, 465, 4500

Portegies Zwart S. F., McMillan S. L. W., Gieles M., 2010, ARA&A, 48, 431

Reimer O. et al., 2007, preprint (arXiv:0710.3418)

Rogers H., Pittard J. M., 2014, MNRAS, 441, 964

Rosen A. R., Lopez L. A., Krumholz M. R., Ramirez-Ruiz E., 2014, MNRAS, 442, 2701

Rybicki G. B., Lightman A. P., 1979, Radiative Processes in Astrophysics. Wiley, New York

Salem M., Bryan G. L., 2014, MNRAS, 437, 3312

Selman E., Melnick J., Bosch G., Terlevich R., 1999, A&A, 347, 532

Sharma P., Roy A., Nath B. B., Shchekinov Y., 2014, MNRAS, 443, 3463

Silich S., Tenorio-Tagle G., 2013, ApJ, 765, 43

Simpson C. M., Pakmor R., Marinacci F., Pfrommer C., Springel V., Glover S. C. O, Clark P. C., Smith R. J., 2016, ApJ, 827, 29

Solomon P. M., Rivolo A. R., Barrett J., Yahil A., 1987, ApJ, 319, 730

Tibaldo L., Grenierb I. A., Fermi LAT collaboration, 2013, Nucl. Phys. B (Proc. Suppl.), 239, 70

Townsley L. K., Broos P. S., Feigelson E. D., Brandl B. R., Chu Y., Gamire G. P., Pavlov G. G., 2006, ApJ, 131, 2140

Valle J. P., 1993, ApJ, 419, 670

Vasiliev E. O., Shchekinov Y., Nath B. B., 2017, MNRAS, 468, 2757

Weaver R., McCray R., Castor J., Shapiro P., Moore R., 1977, ApJ, 218, 377

Wiener J., Pfrommer C., Oh S. P., 2017, MNRAS, 467, 906

Wright N. J., Drake J. J., Drew J. E., Vink J. S., 2010, ApJ, 713, 871

Yadav N., Mukherjee D., Sharma P., Nath B. B., 2017, MNRAS, 465, 172

Yang R.-z., Aharonian F., 2017, A&A, 600, A107

Yang R.-z., de Oña Wilhelmi E., Aharonian F., 2018, A&A, 611, A77

APPENDIX A: DEPENDENCE OF γ-RAY LUMINOSITY ON THE SPATIAL EXTENT OF SIMULATION BOX

While calculating the non-thermal luminosities (γ-ray and radio), we integrate emissivity over the entire simulation box. Since CRs diffuse out from the bubble, the luminosities may increase with the box size. To check this, here we estimate the γ-ray luminosity up to a variable distance r and display the results in Fig. A1 for model ISH.

The smaller points denote $w = 0.1$ and bigger points denote $w = 0.5$, and the point styles stand for different value of $\kappa_{\rm cr}$. We find that the γ-ray luminosity increases with r (distance up to which the emission is calculated), especially for a large $\kappa_{\rm cr}$. This is expected because a larger $\kappa_{\rm cr}$ increases the CR energy density at larger dis-

tance (Aharonian & Atoyan 1996). However, as the density drops with distance, the luminosity stabilizes beyond a box size of $\gtrsim$ 250 pc, making our results presented here robust.
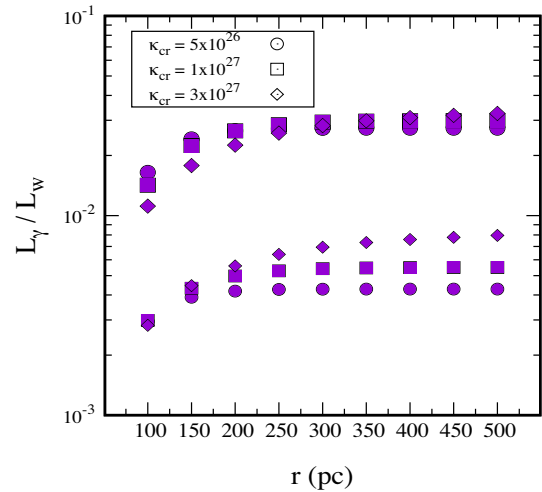

Figure A1. The γ-ray luminosity (normalized w.r.t $L_{\rm w} = 5 \times 10^{38}$ erg s^{-1}) as a function of r (distance from the star cluster up to which the emission is calculated) at $t_{\rm dyn} = 3$ Myr for the model ISH. The smaller points stand for $w = 0.1$ (CR injection fraction) and bigger points for $w = 0.5$ (definition is given in Section 4.3), and the point style represents different $\kappa_{\rm cr}$. Figure shows that γ-ray luminosity stabilizes beyond a box size of $R_{\rm box} \gtrsim 250$ pc.

APPENDIX B: NUMERICAL CONVERGENCE

We present resolution study for our 1D fiducial model in Fig. B1. The dashed curves (IWD model without TC) show that L_γ is converged if the grid resolution $\Delta r \lesssim 0.061$ pc (i.e. grid number $\gtrsim$ 4096). The difference in γ-ray luminosity between low ($\Delta r \approx$ 0.5 pc) and high ($\Delta r = 0.03$ pc) resolution runs is a factor of ≈ 4. For the runs with TC (solid curves), L_γ is almost independent of grid resolution. The difference between with and without TC in the high-resolution case is indistinguishable. It suggests including TC while studying the two-fluid model.

The right panel shows the X-ray luminosity (with TC) for five different resolutions. For ISH model, a low-resolution run causes large cooling losses (see e.g. Yadav et al. 2017) resulting in a smaller $L_{\rm x}$. In IWD model, the bubble is CR dominated which does not cool as efficiently as thermal fluid, results in a weaker dependence on Δr than the ISH case. This figure shows that for IWD model $L_{\rm x}/L_{\rm w} \lesssim 10^{-4}$.

For our 3D runs, $\Delta r \approx 0.79$ pc (for $|x, y, z| \geq 5$ pc) which is much larger than the spatial resolution used in our 1D simulations ($\Delta r \approx 0.06$ pc). We have included TC in order to get a numerically converged L_γ. However, $L_{\rm x}$ is underestimated at this resolution because of the reason discussed above. The qualitative results of 3D runs are consistent with 1D runs.
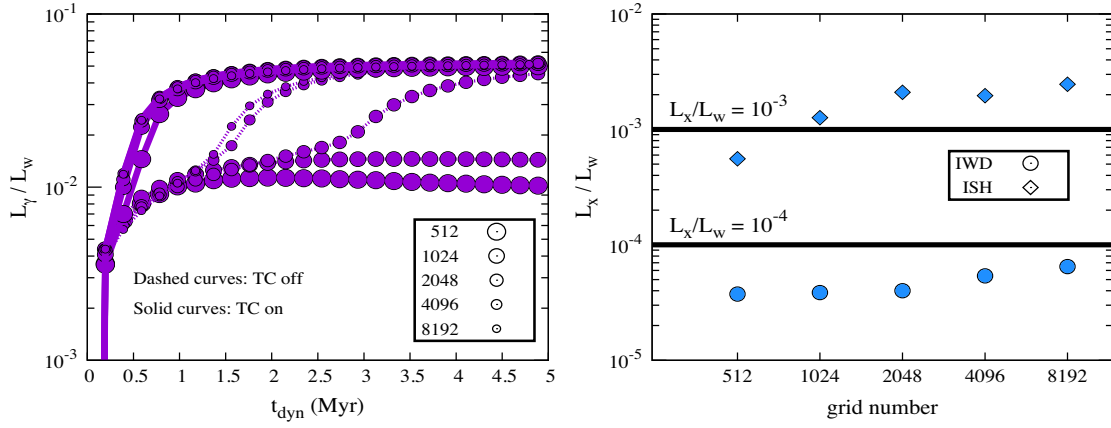
Figure B1. Resolution study for our 1D fiducial model. Left panel: The time evolution of L_γ in IWD model for five different grid resolutions (fiducial resolution $\Delta r \simeq 0.061$ pc i.e. $n_{grid} = 4096$ and the box size is 250 pc) where the size of the circle is proportional to grid spacing (Δr). Figure shows that for a low-resolution run (i.e. $\Delta r > 0.061$ pc), L_γ is converged if TC is on. Right panel: Dependence of L_x (with TC) on grid number ($\propto 1/\Delta r$). The circle and diamond symbols stand for IWD and ISH models, respectively, at 3 Myr. This figure shows that for IWD model $L_x/L_w \lesssim 10^{-4}$.

This paper has been typeset from a TeX/LaTeX file prepared by the author.